nature portfolio

https://doi.org/10.1038/s41563-022-01329-8

Supplementary information

Nuclear spin polarization and control in hexagonal boron nitride

In the format provided by the authors and unedited

Supplementary Information for "Nuclear spin polarization and control in hexagonal boron nitride"

Xingyu Gao,[1] Sumukh Vaidya,[1] Kejun Li,[2] Peng Ju,[1] Boyang Jiang,[3] Zhujing Xu,[1] Andres E. Llacsahuanga Allcca,[1] Kunhong Shen,[1] Takashi Taniguchi,[4] Kenji Watanabe,[5] Sunil A. Bhave,[3,6,7] Yong P. Chen,[1,3,6,7,8] Yuan Ping,[9] and Tongcang Li[1,3,6,7,*]

[1] *Department of Physics and Astronomy, Purdue University, West Lafayette, Indiana 47907, USA*

[2] *Department of Physics, University of California, Santa Cruz, CA, 95064, USA*

[3] *Elmore Family School of Electrical and Computer Engineering, Purdue University, West Lafayette, Indiana 47907, USA*

[4] *International Center for Materials Nanoarchitectonics, National Institute for Materials Science, 1-1 Namiki, Tsukuba 305-0044, Japan*

[5] *Research Center for Functional Materials, National Institute for Materials Science, 1-1 Namiki, Tsukuba 305-0044, Japan*

[6] *Purdue Quantum Science and Engineering Institute, Purdue University, West Lafayette, Indiana 47907, USA*

[7] *Birck Nanotechnology Center, Purdue University, West Lafayette, IN 47907, USA*

[8] *WPI-AIMR International Research Center for Materials Sciences, Tohoku University, Sendai 980-8577, Japan*

[9] *Department of Chemistry and Biochemistry, University of California, Santa Cruz, CA, 95064, USA*

(Dated: July 1, 2022)

I. SAMPLE PREPARATION

hBN nanosheets were exfoliated from a high-quality hBN single crystal synthesized by a high-pressure process to 10-100 nm thick with tapes and transferred onto a Si substrate at 80 °C. To perform ion implantation, we mounted the sample in a home-built ion implanter based on an ion source from PSP Vacuum Technology. The chamber pressure was first pumped to 10^{-7} torr to get rid of oxygen residue, and then increased to 10^{-4} torr by filling with a pure helium gas. The ion implantation was operating at this pressure while a current meter was connected to the conductive sample mount to monitor the ion current and estimate the dose density. The sample was implanted with 2.5 keV helium ions with a dose density of 10^{14} cm^{-2}.

For fabricating the microwave coplanar waveguide (Figure S1(a)), a photoresist was first spun on a sapphire wafer. Then, the photoresist corresponding to the metallic parts of the microwave waveguide was exposed by a Heidelberg DWL66FS laser writer and removed by the developer. After that, we deposited a 10 nm Ti film as the adhesion layer. Then a 300 nm silver film was deposited over the whole area with an e-beam evaporator. At the end, a liftoff process removes the silver film between the center and the ground conducting region of the waveguide.

The hBN nanoflakes with spin defects were transferred onto the silver coplanar waveguide (CPW) using a stamp consisting of a thin polycarbonate (PC) film mounted on a polydimethylsiloxane (PDMS) block on a glass slide. The hBN flakes and PC stamp were

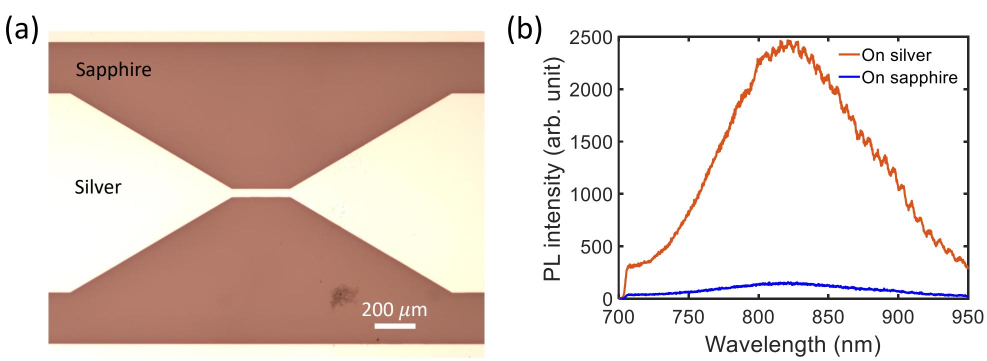

Figure S1. (a) Optical image of the coplanar waveguide. (b)Emission spectra of V_B^- defects under 3 mW laser excitation before (on a Si substrate) and after being transferred to the silver waveguide.

* tcli@purdue.edu

aligned and made contact by using a micropositioner under a microscope. The temperature was raised up to 80 °C to make hBN flakes adhere to the PC film as it was lifted off the substrate. Then the silver CPW was placed on the heater and aligned with hBN flakes. After we made the PC stamp and CPW into contact, the temperature was slowly heated up to 150 °C, which allowed the PC film to melt and attach onto the CPW. Finally, we lifted off the glass slide with the PDMS block and used chloroform to dissolve the PC film from the CPW. On the silver coplanar waveguide, the PL intensity of hBN V_B^- defects was enhanced by approximately 17 times (Figure S1(b)) [1]. All data shown in the main text were taken from the same hBN nanosheet.

II. V_B^- DEFECTS AND ELECTRON SPIN DENSITY

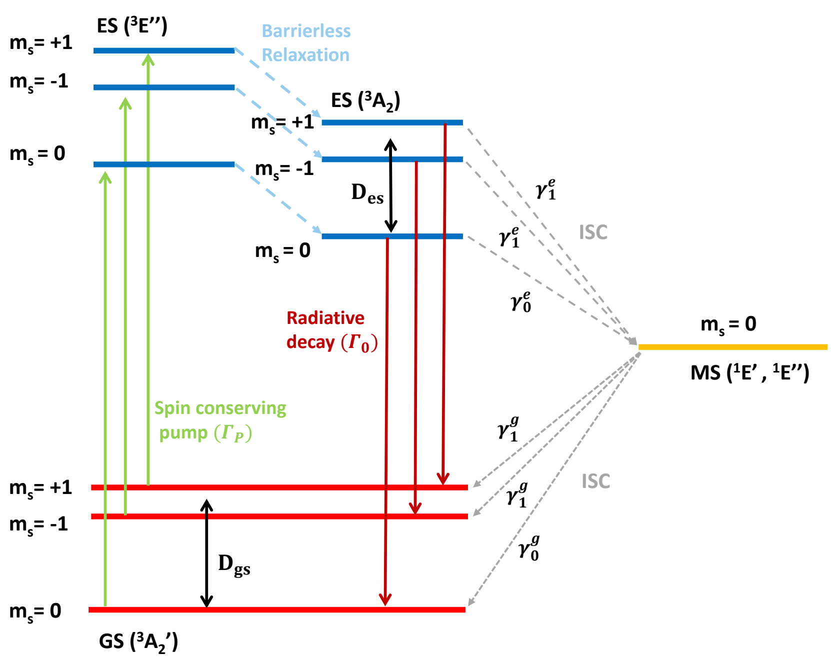

Figure S2. Energy level diagram of the V_B^- defect in hBN [2, 3].

In this work, our ODMR and ODNMR experiments are based on an ensemble of negatively charged boron vacancy defects (V_B^-) in hBN. The energy level diagram of the V_B^- is shown in Figure S2 [2, 3]. The optical cycle includes: laser excitation from the $^3A_2'$ triplet ground state (GS) to a triplet $^3E''$ excited state (green solid lines); non-barrier relaxation from $^3E''$ with a higher symmetry (D_{3h}) to a lower-symmetry (C_{2v}) $^3A_2$ excited state (light blue dashed lines); spin conserving radiative decay (dark red solid lines) from the ${}^3A_2$ excited state to the ${}^3A_2'$ ground state ; and a non-radiative dacay channel through inter system crossing (ISC, gray dashed lines). Due to electron spin-spin interaction, the ${}^3A_2'$ ground state and the ${}^3A_2$ excited state have zero field splittings $D_{gs} = 3.5$ GHz and $D_{es} = 2.1$ GHz, respectively. The PL decay rates are spin dependent and have been demonstrated to be $\gamma_0^e = 1.01$ ns^{-1} and $\gamma_1^e = 2.03$ ns^{-1} [3]. Our first principles DFT calculation provides the spin density of the ${}^3A_2'$ ground state, the ${}^3E''$ excited state and the ${}^3A_2$ excited state, as depicted in Figure S3. The spin density of the ${}^3A_2$ excited state shows a reduction of the symmetry, which will has an impact on the electron-nuclear spin hyperfine interaction in the excited state (see Section III).

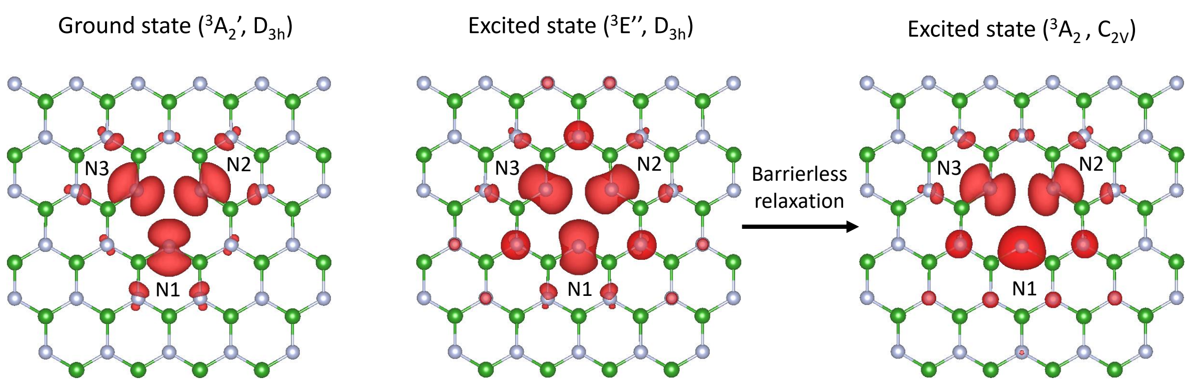

Figure S3. Simulated spin density for ground state and excited states.

III. AB INITIO CALCULATION OF THE HYPERFINE INTERACTION

We use the open source plane-wave code Quantum Espresso (QE) [4] and the Vienna Ab-initio Simulation package (VASP) [5] to calculate hyperfine parameters and compare the results. The hyperfine interaction between nuclear spin and electron spin includes the isotropic (Fermi contact) term at the nucleus site N and the anisotropic dipole-dipole interaction term near the nucleus site N

$$A_{iso}(N) = \frac{2\mu_0}{3} g_e \mu_e g_N \mu_N \rho_{\text{spin}}(\mathbf{R}) \tag{1}$$

$$A_{aniso}(N) = \frac{\mu_0}{4\pi} g_e \mu_e g_N \mu_N \int d^3r \rho_{\text{spin}}(\mathbf{r}) \frac{3\cos^2\theta - 1}{2r^3} \tag{2}$$

where μ_0 is the the permeability of vacuum, g_e is the electron Landé g-factor, μ_e is the Bohr magneton, g_N is the Landé g factor of nucleus, μ_N is the nuclear magneton, $\mathbf{r}$ is the displacement between electron at $\mathbf{r}_e$ and nucleus at $\mathbf{R}$, ρ_{spin} is the spin density, and θ is the angle between r and symmetry axes [6, 7]. g_N is the input in our calculations that is taken from Ref. [8].

Both ground-state and excited-state hyperfine parameters are calculated in this work. We benchmark our calculation by comparing the ground state hyperfine parameters with previous experiment [9] and theoretical results [10], which shows good agreement in Table S1. The ground state ($^3A_2'$) hyperfine parameters also have three-fold rotation symmetry, consistent with the structure symmetry of $\mathrm{V_B^-}$ defect [9]. The excited state ($^3A_2$) hyperfine parameters, on the other hand, shows one N different from the other two. This indicates the structure symmetry of $\mathrm{V_B^-}$ in the excited state reduces to C_{2v} or lower from D_{3h}, which is through a barrierless relaxation process ($^3E'' \rightarrow {}^3A_2$) with a short relaxation time in ps [2].

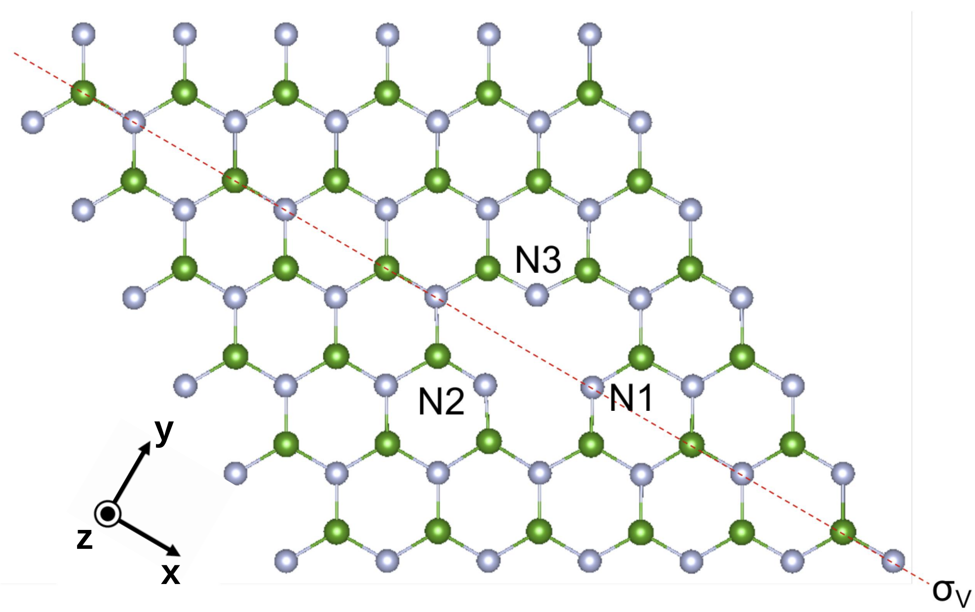

Figure S4. hBN lattice with a V_B^- defect used to study the HFI parameters. N1, N2 and N3 are the three atoms whose hyperfine parameters are calculated. σ_{V} is the mirror symmetry plane that belongs to both D_{3h} and C_{2v} point groups, which describe the ground state $^3A_2'$ and excited state $^3A_2$ of $\mathrm{V_B^-}$ [2], respectively. The z-axis is perpendicular to the hBN flake. The x-axis is parallel to the mirror symmetry plane.

Table S1. Hyperfine parameters of V_B^-. The applied-field direction (quantization axis) is in out-of-plane (z-axis) in our experiment. Our calculated hyperfine parameters in this table are rearranged by rotating the N atom site vector to symmetry axis [11], as can be seen in Figure S4. GS stands for the ground state, and ES stands for the excited state. We found consistent results by using VASP and QE with differences less than 1 MHz.

	Site	A_{xx} (MHz)	A_{yy} (MHz)	A_{zz} (MHz)	A_{xy} (MHz)
Calc. [10]	N3	80.219	57.486	47.957	19.687
	N1	46.110	91.571	47.935	-0.004
	N2	80.202	57.479	47.935	-19.687
This calc. (GS $^3A_2'$, QE)	N1	46.944	90.025	48.158	0.000
	N2	79.406	58.170	48.159	-18.391
	N3	79.406	58.170	48.159	18.391
This calc. (GS $^3A_2'$, VASP)	N1	46.355	89.222	47.555	0.000
	N2	78.655	57.522	47.555	-18.302
	N3	78.655	57.522	47.555	18.302
This calc. (ES $^3E''$, VASP)	N1	24.915	45.972	39.283	0.000
	N2	38.323	45.972	36.403	-1.663
	N3	38.323	45.972	36.403	1.663
This calc. (ES $^3A_2$, QE)	N1	2.850	2.700	41.685	0.000
	N2	46.398	53.140	43.027	-5.839
	N3	46.222	52.888	42.889	5.773
This calc. (ES $^3A_2$, VASP)	N1	3.621	3.464	42.752	0.000
	N2	45.570	52.339	42.185	-5.862
	N3	45.541	52.301	42.161	5.854

IV. SIMULATION OF NUCLEAR SPIN POLARIZATION

In this section, we decribe how the optical pumping and level anticrossing help to polarize nuclear spins in hBN. We use a numerical model that incorporates a spin triplet ground state, a spin triplet excited state and a spin singlet metastable state. Here, the nonradiative decay channel via the two singlet metastable states ^1E and $^1A_1$ is simplified by using only one state.

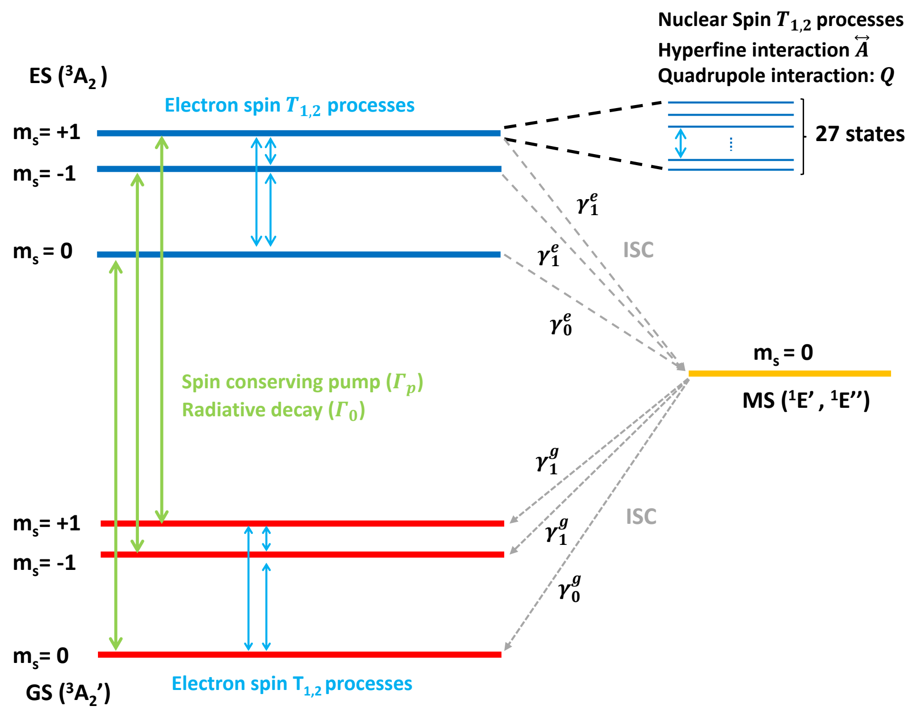

Figure S5. Simplified energy level diagram of the V_B^- defect in hBN used for nuclear spin polarization simulation. This includes a triplet ground state ($^3A_2'$), a triplet excited state ($^3A_2$) and a singlet metastable state ($^1E'$, $^1E''$). Due to the electron-nuclear HFI and QI, each electronic state ($m_s = 0, 1, -1$) splits into non-degerate states. This gives a totally 189 states for the coupled electron-nuclear spin system. Here, the $^3E'$ triplet excited state is ignored since it has negligible effect on spin polarization, owing to its barrierless decay (sub-ps) to the $^3A_2$ excited state.

This gives a total of seven electron spin states for a V_B^- defect. For the nuclear spin states, we consider that the three ^{14}N nuclei surrounding the defect are coupled to the electron spin via the hyperfine interaction. This yields 27 nuclear spin sublevels. Combined with the 7 electronic levels, we get a total of 189 states. The ground state and excited state Hamiltonian of the system include electron spin-spin interaction, electron-nuclear hyperfine interaction, electron and nuclear spin Zeeman splitting, and nuclear spin quadrupole interation. Both of the Hamiltonian take the form of

$$\begin{aligned} H_{gs(es)} =& D[S_z^2 - S(S+1)/3] + \sum_{j=1,2,3} \mathbf{S}\mathbf{A}_j\mathbf{I}_j + \gamma_e B_0 S_z \\ &- \sum_{j=1,2,3} \gamma_n B_0 I_{zj} + \sum_{j=1,2,3} Q_j(I_{zj}^2 - I_j(I_j+1)/3). \end{aligned} \tag{3}$$

Here D and E are the ZFS parameters, γ_e is the electron gyromagnetic ratio, and $\vec{B}$ is the magnetic field. Q_j denotes the nuclear Quadrupole term, γ_N is the ^{14}N nuclear gyromagnetic ratio. The vector operators $\vec{S}$ are the spin-1 operators for the electron spin, and the $\vec{I}_i$ are the spin-1 operators for the nuclear spin. $\mathbf{A}_i$ denotes the hyperfine tensor operator for the three ^{14}N nuclei under consideration. The full Hamiltonian is a combination of the ground state and excited state Hamiltonian, which operates in a 189 dimensional Hilbert space. It is noted that the Hamiltonian of the metastable singlet state is a constant, and thus it is not shown in the full Hamiltonian. The effect of the metastable state will be included in terms of the Lindblad superoperator in the master equation as will be discussed below.

The evolution of the density matrix of the state can be modeled by using the Lindblad master equation [12–14]:

$$\frac{\partial \rho}{\partial t} = -\frac{i}{\hbar}[\hat{H}, \rho] + \hat{L}\rho \tag{4}$$

Here $\hat{H}$ is the full Hamiltonian of the combined system, and $\hat{L}$ is the Lindblad superoperator. This equation is used to describe depopulation and decoherence processes in open quantum

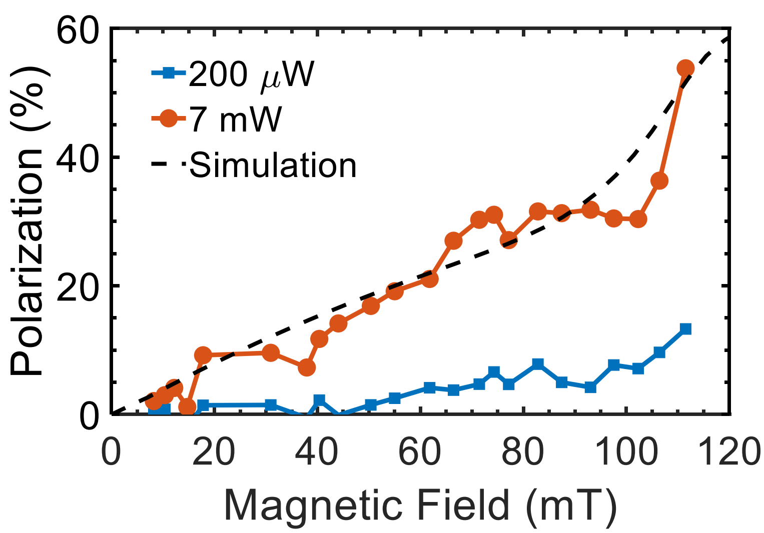

Figure S6. Simulated nuclear spin polarization as a function of magnetic field. The calculation is based on the diagram shown in Figure S5. The inter system crossing rates play an important role in the final value of nulcear spin polarization. Here we use $\gamma_1^e = 2.03\ ns^{-1}$ and $\gamma_0^e = 1.01\ ns^{-1}$ that are taken from ref.[3]. We found that when $\gamma_1^g/\gamma_0^g \approx 0.1$, the simulation agrees well with our experimental observation.

systems[12–14]. The full expression of the Lindblad superoperator is as follows:

$$\hat{L}\rho = \sum_k \Gamma_k (L_k \rho L_k^\dagger - \frac{1}{2}\{L_k^\dagger L_k, \rho\}). \tag{5}$$

Here the {} denotes the anticommutator, Γ_k is the transition rate of the process under consideration and operators L_k describe the depopulation, dephasing and decay of the elements of density matrix ρ. $L_k = |j\rangle\langle i|$ denotes a depopulation-type transition from the state $|i\rangle$ to the state $|j\rangle$. The processes well described by this operator are transition between the ground and excited state of the $m_s = 1$ triplet (Spin conserving optical Pumping Γ_p and spin conserving fluorescence Γ), intersystem crossing from the excited to metastable state ($\gamma^e_{0,1}$) and from the metastable to ground state($\gamma^g_{0,1}$) and the electronic and nuclear T_1 type processes (Figure S5). The operator $L_k = |j\rangle\langle j| - |i\rangle\langle i|$ describes all T_2 type processes that lead to spin-spin relaxation and decoherence. This occurs in the nuclear spins as well as the ground and excited states of the electron spin.

We can then obtain the steady state density matrix for the system under time evolution. We define the nuclear spin polarization as follows [15]:

$$P = \frac{\sum_i I^z_i \rho_i}{3\sum_i \rho_i}, \tag{6}$$

where the I^z_i denotes the total z component of the nuclear spin and ρ_i denotes density matrix element related to the total z component in the steady-state ground state density matrix. We transform the density matrix into Fock-Liouville Space and then find the eigenvector of the resultant superoperator matrix [16, 17]. The population of each steady spin state can be extracted from the matrix element, allowing us to calculate the polarization value by using Eq.6 (Figure S6).

V. SIMULATION OF THE NMR TRANSTIONS

The V_B^- defect has a missing boron atom with three equivalent nitrogen atoms as nearest neighbors. The electron of V_B^- defects mainly couples to these three nitrogen nuclear spins via hyperfine interaction. Nitrogen naturally occurs as the ^{14}N isotope with a nuclear spin I = 1 (99.6%). Thus, the ^{15}N isotope is ignored in our simulation. Considering the fact that the three nearest nitrogen nuclei are on the three lattice sites of a triangle structure, these nuclear spins have different transverse hyperfine interaction parameters (A_{xx} and A_{yy}) in the lab coordinate defined by external magnetic fields (Table S1). The number of non-degenerate energy sublevels of the m_s = -1 branch becomes totally 27 in this coupled electron-nuclear spin system (Figure S7, S8). The 27 energy spin sublevels can be assigned into 7 groups represented by the total nuclear spins $m_{I,tot}$. Within each group, there are multiple spin sublevels with slightly different energies, corresponding to different combinations of the nuclear spin states $(|m_{I,1}\rangle, |m_{I,2}\rangle, |m_{I,3}\rangle)$ that give the same total nuclear spin number $|m_{I,tot} = m_{I,1} + m_{I,2} + m_{I,3}\rangle$. As will be discussed later, increasing the magnitude of the magnetic field > 1 T can reduce the nuclear-nuclear spin interaction mediated by the electron spin, and help to reduce the splitting of the nuclear spin sublevels. As shown in Figure S8(b), in a strong magnetic field (> 1 T), many spin sublevels become nearly degenerate.

The relative transition amplitudes and frequencies of the intra-electronic spin transitions can be calculated from the eigenstates of the Hamiltonian via Fermi's golden rule

$$\Gamma_{i \to f} = | \langle f | H_{drive} | i \rangle |^2, \tag{7}$$

where $\langle f | H_{drive} | i \rangle$ is the matrix element of the perturbation H_{drive} between the final and initial states. And $H_{drive} = A \cdot \mathbf{x} \cos(\omega t)$ is the RF driving Hamiltonian. The matrix elements $\Gamma_{i \to f}$ give the relative strength of the transition at the energy $E_m - E_n$. These are plotted for various values of the magnetic field in Figure S9.

In a weak external magnetic field (B $\ll 1$ T), the large electron-mediated nuclear-nuclear spin interaction leads to a rich feature of nuclear spin transitions (Figure S9). The allowed nuclear spin transitions contain a large number of transition frequencies ranging over a range more than ten MHz. By increasing the magnetic field, we expect to observe a decrease of the number of nuclear spin transition lines. In a strong magnetic field ($\gg 1$ T), the number of transition frequencies decreases to only two for each electron spin branch ($m_s = 0, \pm 1$), which agrees with the observation using the conventional ESR spectrometer at 3.3 T in a former report [18].

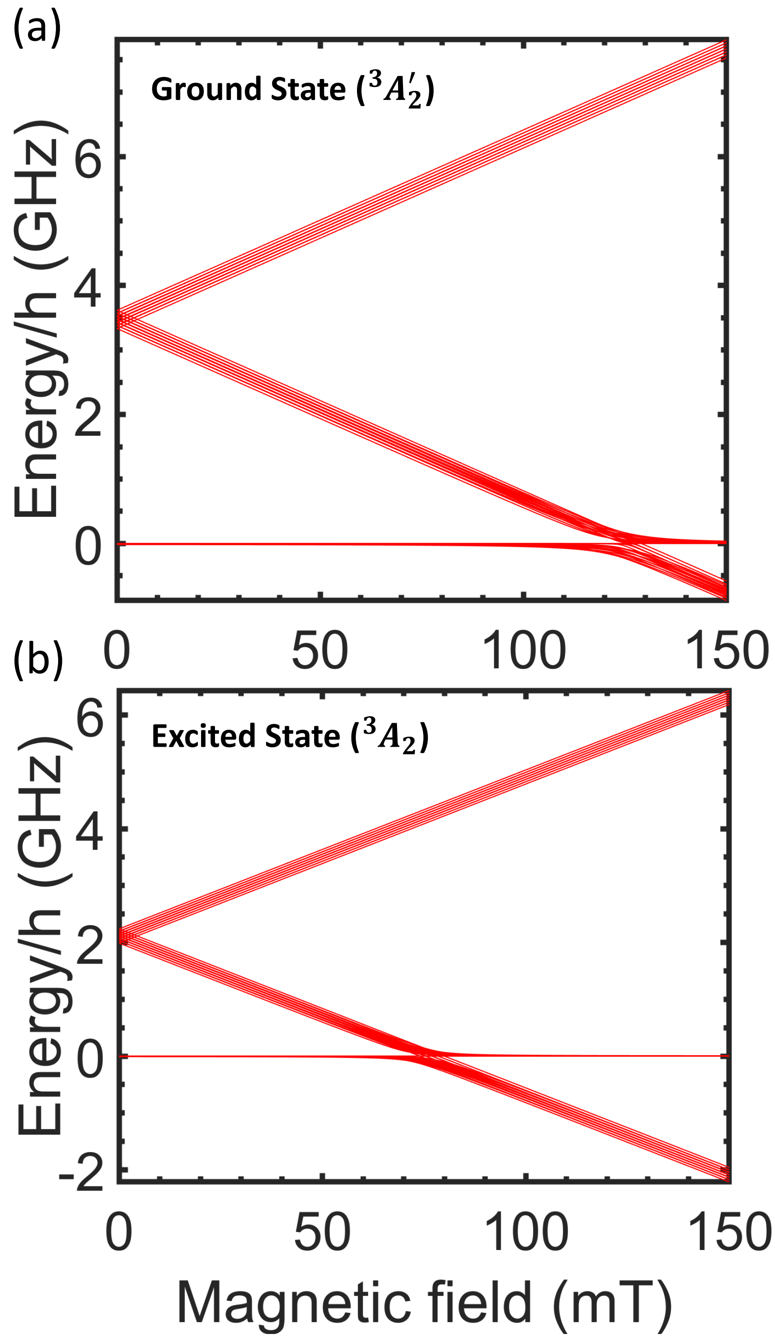

Figure S7. Energy levels in the (a) ground state ($^3A_2'$) and (b) excited state ($^3A_2$) of V_B^- defects as a function of magnetic field.

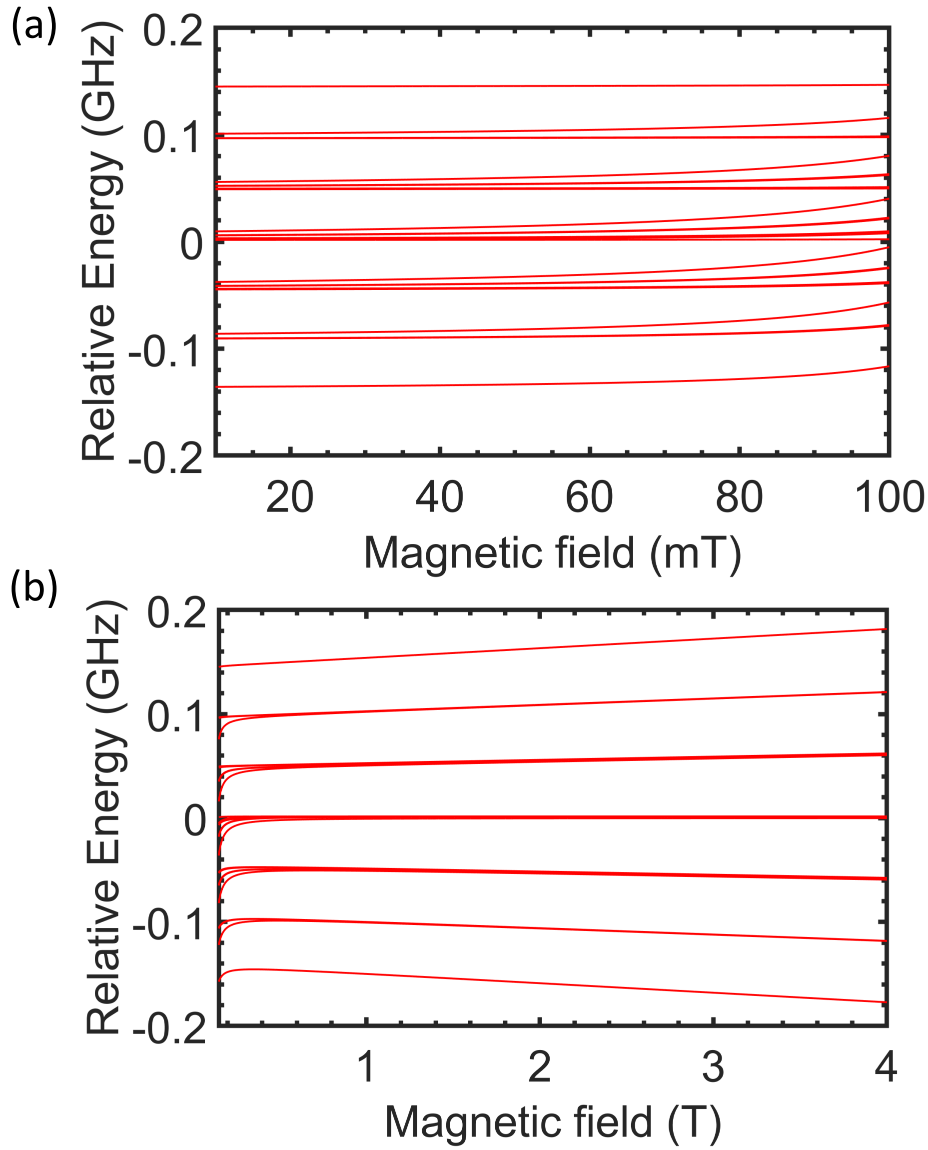

Figure S8. Relative energy levels of the m_s = -1 branch in the ground state of V_B^- defects. For obtaining the curves, the center frequency is fixed at 0.

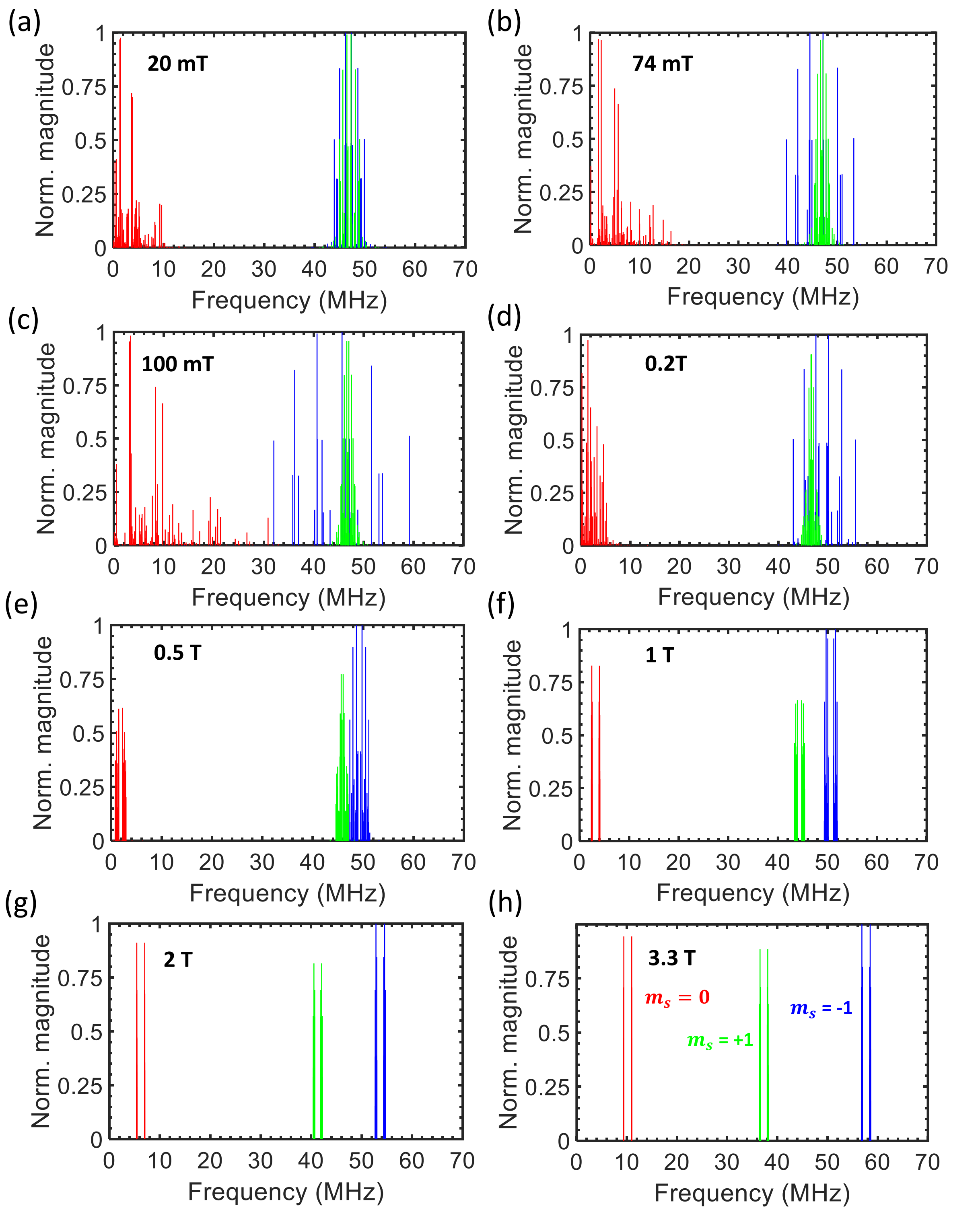

Figure S9. Nuclear spin transitions in different magnetic fields: (a) 20 mT; (b) 74 mT (c) 100 mT (d) 0.2 T (e) 0.5 T (f) 1T (g) 2 T (h) 3.3 T. Red, green and blue lines represent the electron spin states with $m_s = 0$,+1,-1, respectively.

VI. PULSED ODMR MEASUREMENTS

To get access to the spin dynamics of the V_B^- defects and to further control the nuclear spins using the V_B^-, we perform pulsed ODMR measurements. By applying microwave pulses resonantly of variable length, we coherently manipulate the electron spin state via Rabi oscillation. Figure S10(a) shows a Rabi oscillation driving with a 0.35 W microwave at 74 mT. A characteristic frequency $f = 21.9$ MHz is observed along with a depahsing time $T_2^* = 96$ ns. In addition, using the microwave π-pulse known from the Rabi experiment, we measure the T_1 relaxation time of 14.0 μs (Figure S10(b)).

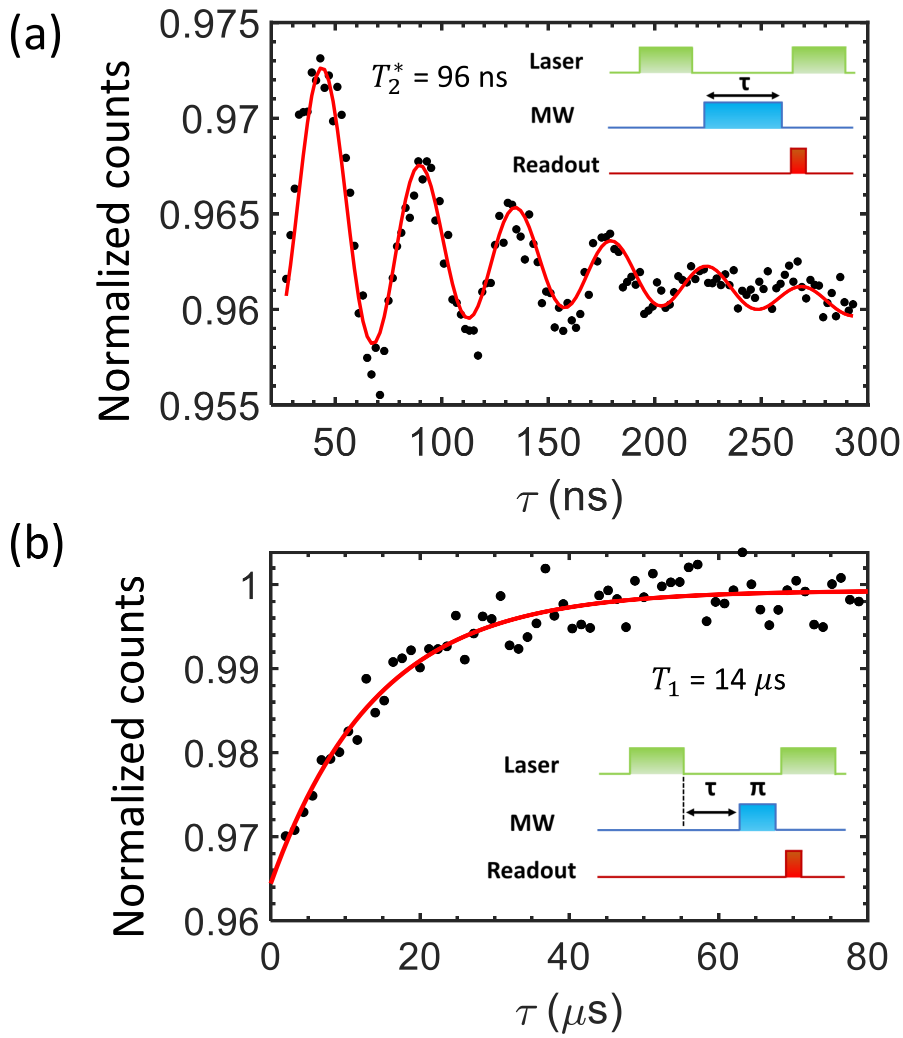

Figure S10. Pulsed ODMR measurements. (a) Rabi oscillation. The fitting result shows a Rabi frequency at 21.9 MHz. (b) T_1 measurement using the π-pulse known from the Rabi experiment. The magnetic field is 74 mT. The microwave power is $P_{MW} = 0.35$ W.

VII. ENHANCEMENT OF ^{14}N NUCLEAR GYROMAGNETIC RATIO NEAR LEVEL ANTICROSSING

Based on second-order perturbation theory, the gyromagnetic ratio of the nuclear spins that couple to the spin defects can be effectively enhanced in the presence of a magnetic field near the GSLAC [19, 20]. Such an enhancement will speed up initialization, coherent control and readout of the nuclear spins. The enhancement factor $\alpha \equiv \gamma_{N,eff}/\gamma_{N,bare}$ increases dramatically around GSLAC but remains at a relatively large value over a large range of magnetic even at ESLAC.

In our nuclear spin control measurement, we observe a fast controlling rate which is supposed to originate from the enhancement of nuclear spin gyromagnetic ratio. To estimate the expected enhancement, here we numerically calculate the enhancement factor α as a function of magnetic field.

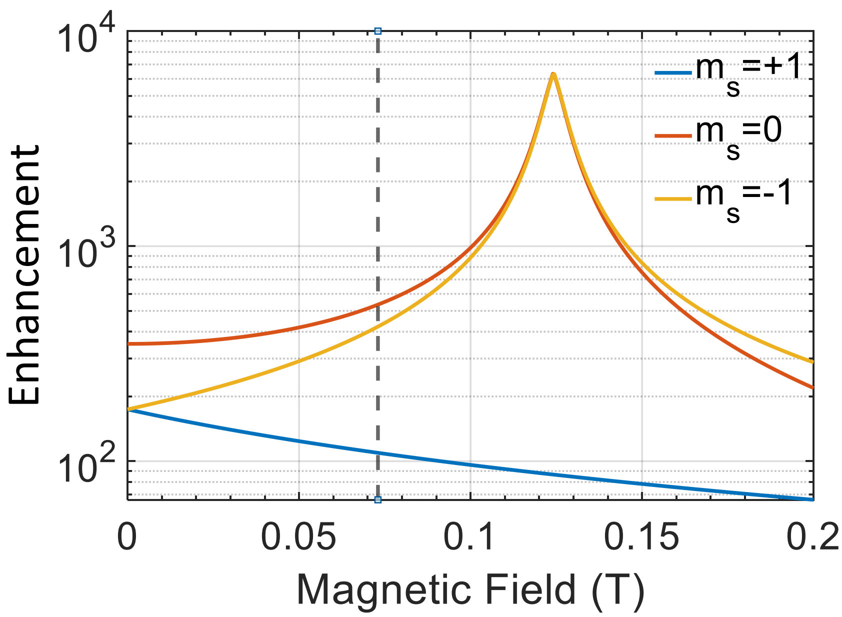

Figure S11. Enhancement of Gyromagnetic Ratio in the ground state of V_B^- center in hBN. The dashed line marks the magnetic field where we perform the ODNMR measurements.

To calculate the enhancement factor, we neglect the nuclear-nuclear spin interaction as it is much weaker than the electron-nuclear coupling. In this context, we can consider the gyromagnetic ratio enhancement of each ^{14}N nuclear spin individually. We write the Hamiltonian of a single nuclear spin coupled to a spin-1 electron ground state in the presence of an external magnetic field. Here we ignore the nuclear spin quadrupole interaction since Q $\ll D - \gamma_e B$. The secular part of the Hamiltonian takes the form:

$$H = DS_z^2 + \gamma_e B_z S_z - \gamma_N B_z I_z + A_{zz} S_z I_z, \tag{8}$$

and under the rotating wave approximation, the nonsecular part can be written as:

$$H_1 = A_{xx} S_x I_x + A_{yy} S_y I_y \cong \frac{A_{xx} + A_{yy}}{4}(S_+ I_- + S_- I_+), \tag{9}$$

where $I_\pm = I_x \pm iI_y, S_\pm = S_x \pm iS_y$ and A_{ij} denote the components of the hyperfine tensor. This nonsecular Hamiltonian leads to the coupling between the states $|m_s, m_I\rangle = |0,1\rangle \longleftrightarrow |1,0\rangle$ and between $|0,0\rangle \longleftrightarrow |-1,1\rangle$. This is then diagonalised by rotating via unitary transformation $U = e^{-i(\sigma_y^- \nu^- + \sigma_y^+ \nu^+)}$. The matrices in the exponent are $\sigma_y^+ = i(|1,0\rangle\langle 0,1| - |0,1\rangle\langle 1,0|)$ and $\sigma_y^- = i(|0,0\rangle\langle -1,1| - |-1,1\rangle\langle 0,0|)$. The rotation angles are given by:

$$tan(2\nu^+) = \frac{A_{xx} + A_{yy}}{D + \gamma_e B_z + \gamma_N B_z} \tag{10}$$

$$tan(2\nu^-) = \frac{-(A_{xx} + A_{yy})}{D - \gamma_e B_z - \gamma_N B_z - A_{zz}} \tag{11}$$

Following this rotation we get the gyromagnetic ratio enhancement factors for the three electron spin states as follows:

$$\alpha_{+1} = cos(\nu^+) - \frac{\gamma_e}{\gamma_N} sin(\nu^+) \tag{12}$$

$$\alpha_0 = cos(\nu^+)cos(\nu^-) + \frac{\gamma_e}{\gamma_N} sin(\nu^+ - \nu^-) \tag{13}$$

$$\alpha_{-1} = cos(\nu^-) + \frac{\gamma_e}{\gamma_N} sin(\nu^-). \tag{14}$$

We then plot these values to see the expected result of large enhancement for the $m_S = 0, -1$ states but small enhancement for the $m_s = +1$ state. This is due to the fact that the $m_S = 0, -1$ states interact via the Hyperfine tensor at the Level Anticrossing whereas the $m_s = +1$ does not.

As shown in Figure S11, the nuclear spin gyromagnetic field remains at a large value within a broad range of the magnetic field. At ESLAC, the enhancement of the nuclear spins coupled to $m_s = -1$ state is predicted to be around 420. With nearly the same RF or MW driving power at 0.35 W, the Rabi frequency of the nuclear spin and electron spin are 0.847 MHz (Figure 4 in the main text) and 21.9 MHz (Figure S10(a)), respectively. Therefore, the enhancement is measured to be approximately 351, which is close to the theoretical prediction.

VIII. ELECTRON-MEDIATED NUCLEAR-NUCLEAR SPIN COUPLING

In our coupled electron-nuclear spin system, the electron spin of V_B^- are mainly coupled to the three neighboring ^{14}N nuclear spins. Without the electron, bare nuclear-nuclear spin interaction is very weak since $(\gamma_N/\gamma_e)^2 \sim 10^{-8}$. However, by coupling to the V_B^- electron spin via HFI, the nuclear spins can be indirectly coupled to each other [21, 22], making the nulcear spin energy sublevels non-degenerate according to the second-order perturbation. To gain more insight on this electron mediated nuclear spin coupling mechanism, we describe this coupling dynamics by obtaining the effective electron-mediated nulcear-nuclear spin interaction Hamiltonian. Here we utilize the second order perturbation theroy to adiabatically eliminate the electron spin from the original Hamiltonian, which is valid when $|D - \gamma_e B| \gg \gamma_N B$, $\overleftrightarrow{\mathbf{A}}$. We begin from the Hamiltonian

$$H = \Delta_e S_z + \sum_{j=1,2,3} \Delta_N I_{z,j} + \sum_{j=1,2,3} (A_{zz,j} S_z I_{z,j} + A_{xx,j} S_x I_{x,j} + A_{yy,j} S_y I_{y,j}), \tag{15}$$

where $\Delta_e = \pm D + \gamma_e B_z$ and $\Delta_N = -\gamma_N B_z$ are the splittings of the electron and nuclear energy sublevels, respectively. We separate the Hamiltonian into two parts

$$H = H_0 + V_{ff} \tag{16}$$

where

$$H_0 = \Delta_e S_z + \sum_{j=1,2,3} \Delta_N I_{z,j} + \sum_{j=1,2,3} A_{zz,j} S_z I_{z,j} \tag{17}$$

and

$$V_{ff} = \sum_{j=1,2,3} \frac{A_{tran,j}}{2} (S_+ I_{-,j} + S_- I_{+,j}). \tag{18}$$

Here $A_{tran,j} = (A_{xx,j} + A_{yy,j})/2$ is the transverse hyperfine interaction parameter. To find an effective Hamiltonian that eliminates the electron-nuclear spin flip-flop term V_{ff}, we choose an operator S, such that $[H_0, S] = V_{ff}$. With the operator S, the effective Hamiltonian can be obtained by using Schrieffer-Wolff transformation

$$H_{eff} = e^S H e^{-S} \cong H_0 + \frac{1}{2}[S, V_{ff}]. \tag{19}$$

We choose the operator

$$S = \frac{1}{2} \sum_{j=1,2,3} A_{tran,j} \left(\frac{1}{\Delta_e - \Delta_N \pm A_{zz,j}} S_+ I_{-,j} - \frac{1}{\Delta_e - \Delta_N \pm A_{zz,j}} S_- I_{+,j}\right), \tag{20}$$

for the $m_s = +1$ and $m_s = -1$ branches, respectively. Inserting Eq. 20 into Eq. 19, we obtain the effective Hamiltonian

$$\begin{aligned} H_{-1} = &(D - \gamma_e B) - A_{zz,j} I_{z,j} - \sum_{j=1,2,3} \gamma_N B_z I_{z,j} \\ &+ \frac{1}{4} \sum_{j \neq k} \frac{A_{tran,j} A_{tran,k}}{D - \gamma_e B - \gamma_N B - A_{zz,j}} (I_{-,j} I_{+,k} + I_{+,j} I_{-,k}) \\ &+ \frac{1}{2} \sum_{j=1,2,3} \frac{A_{tran,j}^2}{D - \gamma_e B - \gamma_N B - A_{zz,j}} I_{z,j}, \end{aligned} \tag{21}$$

and

$$\begin{aligned} H_{+1} = &(D + \gamma_e B) + A_{zz,j} I_{z,j} - \sum_{j=1,2,3} \gamma_N B_z I_{z,j} \\ &+ \frac{1}{4} \sum_{j \neq k} \frac{A_{tran,j} A_{tran,k}}{D + \gamma_e B + \gamma_N B + A_{zz,j}} (I_{-,j} I_{+,k} + I_{+,j} I_{-,k}) \\ &- \frac{1}{2} \sum_{j=1,2,3} \frac{A_{tran,j}^2}{D + \gamma_e B + \gamma_N B + A_{zz,j}} I_{z,j}, \end{aligned} \tag{22}$$

for the $m_s = -1$ and $m_s = +1$ branches, respectively. The second last terms in H_{-1} and H_{+1} are the electron-mediated nuclear-nuclear spin couplings.

Based on H_{-1}, we can introduce a nuclear-nuclear spin coupling constant $C_{NN,j,k}$ for the $m_s = -1$ branch in the ground state:

$$C_{NN,j,k} = \frac{1}{2} \left(\frac{A_{tran,j} A_{tran,k}}{D_{GS} - \gamma_e B - \gamma_N B - A_{zz,j}} + \frac{A_{tran,j} A_{tran,k}}{D_{GS} - \gamma_e B - \gamma_N B - A_{zz,k}} \right). \tag{23}$$

From our calculated hyperfine parameters for GS ($^3A_2'$) with the VASP method as shown in Table S1, we have $A_{tran,1} = 67.789$ MHz, $A_{tran,2} = 68.089$ MHz, $A_{tran,3} = 68.089$ MHz. Thus $A_{tran,1} \approx A_{tran,2} = A_{tran,3} = A_{tran} \approx 68$ MHz due to the symmetry of the ground state. When the system is far away from GSLAC, we have $(D_{GS} - \gamma_e B - \gamma_N B - A_{zz,j}) \approx (D_{GS} - \gamma_e B - \gamma_N B - A_{zz,k}) \approx (D_{GS} - \gamma_e B)$. Thus the absolute value of the nuclear-nuclear spin coupling constant $C_{NN,j,k}$ for the $m_s = -1$ branch in the ground state can be simplified as C_{NN}:

$$C_{NN} = \frac{A_{tran}^2}{|D_{GS} - \gamma_e B|}. \tag{24}$$

It increases when the system is close to the GSLAC, and decreases when the magnetic field is very large. The value of C_{NN} is about 3.4 MHz around ESLAC, and $C_{NN} = 50$ kHz at 3.3 T. In comparison, the direct nuclear spin dipolar coupling strength is $d_{NN} = \mu_0 (\gamma_n)^2 \hbar / (2 r_{NN}^3) =$

34 Hz. The enhancement of the nuclear-nuclear spin coupling due to the electron spin is shown in Figure S12. At ESLAC, the enhancement factor reaches 10^5 and gives a much stronger effective nuclear-nuclear spin coupling strength.

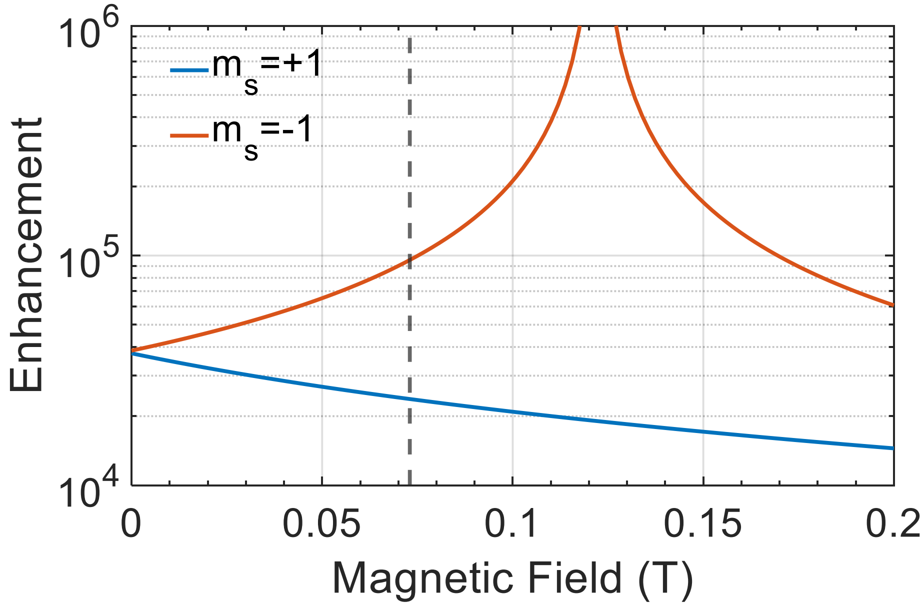

Figure S12. Enhancement of the nuclear-nuclear spin coupling due to the V_B^- electron spin as a function of the magnetic field.

---

[1] Xingyu Gao, Boyang Jiang, Andres E Llacsahuanga Allcca, Kunhong Shen, Mohammad A Sadi, Abhishek B Solanki, Peng Ju, Zhujing Xu, Pramey Upadhyaya, Yong P Chen, Sunil A Bhave, and Tongcang Li. High-contrast plasmonic-enhanced shallow spin defects in hexagonal boron nitride for quantum sensing. *Nano Letters*, 21(18):7708–7714, 2021.

[2] Jeffrey R Reimers, Jun Shen, Mehran Kianinia, Carlo Bradac, Igor Aharonovich, Michael J Ford, and Piotr Piecuch. Photoluminescence, photophysics, and photochemistry of the v b- defect in hexagonal boron nitride. *Phys. Rev. B*, 102(14):144105, 2020.

[3] Simon Baber, Ralph Nicholas Edward Malein, Prince Khatri, Paul Steven Keatley, Shi Guo, Freddie Withers, Andrew J Ramsay, and Isaac J Luxmoore. Excited state spectroscopy of boron vacancy defects in hexagonal boron nitride using time-resolved optically detected magnetic resonance. *Nano Letters*, 22(1):461, 2022.

[4] Paolo Giannozzi, Stefano Baroni, Nicola Bonini, Matteo Calandra, Roberto Car, Carlo Cavazzoni, Davide Ceresoli, Guido L Chiarotti, Matteo Cococcioni, Ismaila Dabo, Andrea Dal Corso, Stefano de Gironcoli, Stefano Fabris, Guido Fratesi, Ralph Gebauer, Uwe Gerstmann, Christos Gougoussis, Anton Kokalj, Michele Lazzeri, Layla Martin-Samos, Nicola Marzari, Francesco Mauri, Riccardo Mazzarello, Stefano Paolini, Alfredo Pasquarello, Lorenzo Paulatto, Carlo Sbraccia, Sandro Scandolo, Gabriele Sclauzero, Ari P Seitsonen, Alexander Smogunov, Paolo Umari, and Renata M Wentzcovitch. QUANTUM ESPRESSO: A Modular and Open-Source Software Project for Quantum Simulations of Materials. *J. Phys.: Condens. Matter*, 21(39):395502, sep 2009.

[5] Georg Kresse and Jürgen Furthmüller. Efficient iterative schemes for ab initio total-energy calculations using a plane-wave basis set. *Phys. Rev. B*, 54(16):11169, 1996.

[6] Chris G Van de Walle and Peter E Bloechl. First-principles calculations of hyperfine parameters. *Phys. Rev. B*, 47(8):4244, 1993.

[7] Mohammad Saeed Bahramy, Marcel HF Sluiter, and Yoshiyuki Kawazoe. Pseudopotential hyperfine calculations through perturbative core-level polarization. *Phys. Rev. B*, 76(3):035124, 2007.

[8] NJ Stone. Table of nuclear magnetic dipole and electric quadrupole moments. *At. Data Nucl. Data Tables*, 90(1):75–176, 2005.

[9] Andreas Gottscholl, Mehran Kianinia, Victor Soltamov, Sergei Orlinskii, Georgy Mamin, Carlo Bradac, Christian Kasper, Klaus Krambrock, Andreas Sperlich, Milos Toth, et al. Initialization and read-out of intrinsic spin defects in a van der waals crystal at room temperature. *Nat. Mater.*, 19(5):540–545, 2020.

[10] Viktor Ivády, Gergely Barcza, Gergő Thiering, Song Li, Hanen Hamdi, Jyh-Pin Chou, Örs Legeza, and Adam Gali. Ab initio theory of the negatively charged boron vacancy qubit in hexagonal boron nitride. *npj Computational Materials*, 6(1):1–6, 2020.

[11] R Beck, PF Meier, and A Schenck. On the change of polarization of positive muons in alkali halides. *Z. Phys. B Condens. Matter.*, 22(2):109–115, 1975.

[12] Laima Busaite, Reinis Lazda, Andris Berzins, Marcis Auzinsh, Ruvin Ferber, and Florian Gahbauer. Dynamic n 14 nuclear spin polarization in nitrogen-vacancy centers in diamond. *Physical Review B*, 102(22):224101, 2020.

[13] Viktor Ivády, Krisztián Szász, Abram L Falk, Paul V Klimov, David J Christle, Erik Janzén,

Igor A Abrikosov, David D Awschalom, and Adam Gali. Theoretical model of dynamic spin polarization of nuclei coupled to paramagnetic point defects in diamond and silicon carbide. *Physical Review B*, 92(11):115206, 2015.

[14] V Jacques, P Neumann, J Beck, M Markham, D Twitchen, J Meijer, F Kaiser, G Balasubramanian, F Jelezko, and J Wrachtrup. Dynamic polarization of single nuclear spins by optical pumping of nitrogen-vacancy color centers in diamond at room temperature. *Physical review letters*, 102(5):057403, 2009.

[15] Laima Busaite, Reinis Lazda, Andris Berzins, Marcis Auzinsh, Ruvin Ferber, and Florian Gahbauer. Dynamic ^{14}N nuclear spin polarization in nitrogen-vacancy centers in diamond. *Phys. Rev. B*, 102:224101, Dec 2020.

[16] Daniel Manzano. A short introduction to the lindblad master equation. *AIP Advances*, 10(2):025106, 2020.

[17] Paola Cappellaro. *Quantum Theory of Radiation Interactions*. Massachusetts Institute of Technology: MIT OpenCourseWare, 2012.

[18] Fadis F Murzakhanov, Georgy V Mamin, Sergei B Orlinskii, Uwe Gerstmann, Wolf G Schmidt, Timur Biktagirov, Igor Aharonovich, Andreas Gottscholl, Andreas Sperlich, Vladimir Dyakonov, and Victor A. Soltamov. Electron-nuclear coherent coupling and nuclear spin readout through optically polarized V_B^- spin states in hBN. *Nano Lett.*, 22(7):2718, 2022.

[19] Mo Chen, Masashi Hirose, Paola Cappellaro, et al. Measurement of transverse hyperfine interaction by forbidden transitions. *Physical Review B*, 92(2):020101, 2015.

[20] S Sangtawesin, CA McLellan, BA Myers, AC Bleszynski Jayich, DD Awschalom, and Jason R Petta. Hyperfine-enhanced gyromagnetic ratio of a nuclear spin in diamond. *New Journal of Physics*, 18(8):083016, 2016.

[21] A. Bermudez, F. Jelezko, M. B. Plenio, and A. Retzker. Electron-mediated nuclear-spin interactions between distant nitrogen-vacancy centers. *Phys. Rev. Lett.*, 107:150503, Oct 2011.

[22] MV Gurudev Dutt, L Childress, L Jiang, E Togan, J Maze, F Jelezko, AS Zibrov, PR Hemmer, and MD Lukin. Quantum register based on individual electronic and nuclear spin qubits in diamond. *Science*, 316(5829):1312–1316, 2007.